Injectable biomimetic liquid crystalline scaffolds enhance muscle stem cell transplantation

Eduard Sleep[a,1], Benjamin D. Cosgrove[b,c,1], Mark T. McClendon[a], Adam T. Preslar[a,d,e,f,g,h], Charlotte H. Chen[i], M. Hussain Sangji[e], Charles M. Rubert Pérez[a,2], Russell D. Haynes[b,3], Thomas J. Meade[d,e,f,g,h], Helen M. Blau[b,1,4,5], and Samuel I. Stupp[a,d,e,i,j,4,5]

[a]Simpson Querrey Institute for BioNanotechnology, Northwestern University, Chicago, IL 60611-2875; [b]Baxter Laboratory for Stem Cell Biology, Stanford University School of Medicine, Stanford, CA 94305-5175; [c]Meinig School of Biomedical Engineering, Cornell University, Ithaca, NY 14853; [d]Department of Chemistry, Northwestern University, Evanston, IL 60208; [e]Department of Biomedical Engineering, Northwestern University, Evanston, IL 60208; [f]Department of Molecular Biosciences, Northwestern University, Evanston, IL 60208; [g]Department of Neurobiology, Northwestern University, Evanston, IL 60208; [h]Department of Radiology, Northwestern University, Evanston, IL 60208; [i]Department of Materials Science and Engineering, Northwestern University, Evanston, IL 60208; and [j]Department of Medicine, Northwestern University, Chicago, IL 60611

Contributed by Helen M. Blau, August 4, 2017 (sent for review November 6, 2016; reviewed by Kristi S. Anseth and Jason A. Burdick)

Muscle stem cells are a potent cell population dedicated to efficacious skeletal muscle regeneration, but their therapeutic utility is currently limited by mode of delivery. We developed a cell delivery strategy based on a supramolecular liquid crystal formed by peptide amphiphiles (PAs) that encapsulates cells and growth factors within a muscle-like unidirectionally ordered environment of nanofibers. The stiffness of the PA scaffolds, dependent on amino acid sequence, was found to determine the macroscopic degree of cell alignment templated by the nanofibers in vitro. Furthermore, these PA scaffolds support myogenic progenitor cell survival and proliferation and they can be optimized to induce cell differentiation and maturation. We engineered an in vivo delivery system to assemble scaffolds by injection of a PA solution that enabled coalignment of scaffold nanofibers with endogenous myofibers. These scaffolds locally retained growth factors, displayed degradation rates matching the time course of muscle tissue regeneration, and markedly enhanced the engraftment of muscle stem cells in injured and noninjured muscles in mice.

biomaterials | scaffold | muscle stem cell | cell delivery | muscle regeneration

Skeletal muscle displays remarkable regenerative capacity under normal physiological circumstances, including acute injuries. However, upon aging (sarcopenia) or disease (muscular dystrophies and cancer-associated cachexia), skeletal muscle progressively loses its regenerative potential and degenerates (1). Since their first anatomic description in 1961 (2), satellite cells (SCs), also known as muscle stem cells (MuSCs) (3, 4), have been postulated to be the main source of adult skeletal muscle regeneration. Genetic lineage tracing, cell ablation, and transplantation experiments have confirmed that SCs, the Pax7-expressing mononuclear cells located under the myofiber basal lamina, are essential to muscle regeneration in mammals (3, 5–10).

Before these advances in the characterization of MuSCs, experiments in the late 1980s focused on muscle progenitor cells (MPCs), or myoblasts, which are mononucleated cells prepared by enzymatic dissociation of skeletal muscle. Myoblasts can fuse with preexisting or regenerating myofibers to rescue certain aspects of muscular dystrophy in mice (11) and were used in human clinical trials as a cell therapy for Duchenne muscular dystrophy (DMD) patients (1, 12–15). Although these clinical trials provided evidence of myoblast integration into the recipient tissue, myoblast contribution was low, owing to poor viability and limited cell migration, and strength recovery outcomes were negligible (1). These deficiencies have been attributed to the limited viability and potency for self-renewal of the injected cells in the patients with DMD (12). The establishment of transgenic systems and surface markers to prospectively isolate MuSCs (1, 3, 7, 16–19) catalyzed the finding that even a single α7-integrin$^+$ CD34$^+$ MuSC can display both self-renewal and differentiation capacity, following transplantation into muscle tissue (3). Given that MuSCs are rare (<5% of all myonuclei) (1, 20), challenges remain in the isolation of therapeutically needed cell numbers. Their expansion in culture is also problematic given that traditional culture conditions lead to abrupt differentiation and loss of their regenerative potential (7). Previously, we engineered hydrogel substrates that mimic the stiffness of muscle tissues and showed they maintain MuSC function in vitro (21) and allow for MuSC expansion in conjunction with a small molecule inhibitor of p38 mitogen-activated protein kinase (22).

Delivery of MuSCs to tissues still remains a translational challenge and technologies that maximize the viability and potency of MuSCs upon transplantation in vivo are needed. Even though multiple systems have been described to generate tissue-engineered forms of skeletal muscle tissue for volumetric muscle defects (reviewed in refs. 23 and 24), injectable cell encapsulation strategies that enhance MuSC transplantation remain undeveloped. We reported earlier on aqueous liquid crystalline solutions of supramolecular peptide

Significance

Most research aiming to achieve muscle regeneration focuses on the biology of "muscle stem cells," but delivery methods that enhance transplantation efficiency of these cells are at early stages. We report on a liquid crystalline scaffold that encapsulates the cells and gels upon injection in vivo without requiring an external stimulus. As a unique structural feature, the scaffold contains nanofibers that align preferentially with surrounding natural muscle fibers. The biomimetic scaffold can have a stiffness that matches that of muscle, has great ability to retain growth factors, and has a biodegradation rate that is compatible with regeneration time scales. Most importantly, the scaffold enhances engraftment efficiency of the cells in injured muscle, and without injury when combined with growth factors.

Author contributions: E.S., B.D.C., M.T.M., A.T.P., C.H.C., M.H.S., C.M.R.P., R.D.H., T.J.M., H.M.B., and S.I.S. designed research; E.S., B.D.C., M.T.M., A.T.P., C.H.C., M.H.S., C.M.R.P., and R.D.H. performed research; E.S., B.D.C., M.T.M., A.T.P., C.H.C., M.H.S., C.M.R.P., T.J.M., H.M.B., and S.I.S. analyzed data; and E.S., B.D.C., M.T.M., A.T.P., M.H.S., H.M.B., and S.I.S. wrote the paper.

Reviewers: K.S.A., Howard Hughes Medical Institute and University of Colorado Boulder; and J.A.B., University of Pennsylvania.

The authors declare no conflict of interest.

Freely available online through the PNAS open access option.

[1]E.S. and B.D.C. contributed equally to this work.

[2]Present address: Department of Chemistry, DePaul University, Chicago, IL 60614.

[3]Present address: Teikoku Pharma USA, San Jose, CA 95131.

[4]H.M.B. and S.I.S. contributed equally to this work.

[5]To whom correspondence may be addressed. Email: hblau@stanford.edu or s-stupp@northwestern.edu.

This article contains supporting information online at www.pnas.org/lookup/suppl/doi:10.1073/pnas.1708142114/-/DCSupplemental.

Downloaded at Palestinian Territory, occupied on December 4, 2021

www.manaraa.com

amphiphile (PA) nanofibers that can be mixed with cells and sheared in electrolytic media to form gels with nanofiber alignment (25). Here we identify some of the physical properties required for the formation of PA-based liquid crystalline solutions and describe the supramolecular crafting of an injectable biomimetic scaffold of PA nanofibers to encapsulate MuSCs as a combined matrix-cell therapy. We sought to design an injectable PA scaffold with the microstructural organization and stiffness of myofibers in muscle (21, 22, 26). We hypothesized that these dual biomimetic features would enhance MuSC transplantation and therapy.

Results

Liquid Crystalline Scaffolds Arise from Solutions with Specific PA Nanostructure Size and Zeta Potential. PAs consisting of an aliphatic palmitoyl tail covalently attached to a peptide sequence self-assemble in solution at neutral pH, typically yielding a suspension of high aspect-ratio nanofibers (27) (Fig. 1*A* and *SI Appendix*, Fig. S1*A*). Upon annealing, certain PA nanofibers elongate effectively to "infinite" length as they reach their thermodynamically stable state, according to PA concentration and ionic strength (28). We have confirmed this for three previously described PAs by imaging them by cryogenic transmission electron microscopy (CryoTEM) before and after annealing. After annealing, it was very hard to find nanofiber ends, especially in the same fiber, making fiber length measurements impossible (*SI Appendix*, Fig. S1 *A* and *B*). We have previously observed that lyotropic liquid crystals made of annealed PA (aPA) solutions contained very long PA nanofibers (25). However, not all aPA solutions displayed liquid crystalline behavior (25). We have also previously observed that by changing the amino acid sequence in the β-sheet-forming region of PA molecules, we could modify the stiffness of the resulting nonannealed PA gels (29). Since we wanted to create liquid crystalline scaffolds varying in stiffness, we first investigated the nanoscale structure of several negatively charged aPAs (Fig. 1*B* and *SI Appendix*, Figs. S2–S6). We found that not all aPAs formed infinite-length nanofibers when dissolved at 13 mM in a salt-containing solution. In fact, C_{16}A3V3E3 formed "short" nanofibers and C_{16}V4A2E3 formed even shorter supramolecular structures (Fig. 1*B*). The PAs that did form long nanofibers, in this case twisted ribbons, were C_{16}V2A4E3, C_{16}V3A3E3, and C_{16}V2A2E2 (Fig. 1*B*). Coincidentally, the 13-mM solutions of these three aPAs were also found to display domains of birefringence, a blueprint of their liquid crystalline state (Fig. 1*C*). Moreover, these three aPA solutions, but not those formed by C_{16}A3V3E3 or C_{16}V4A2E3, could be gelled

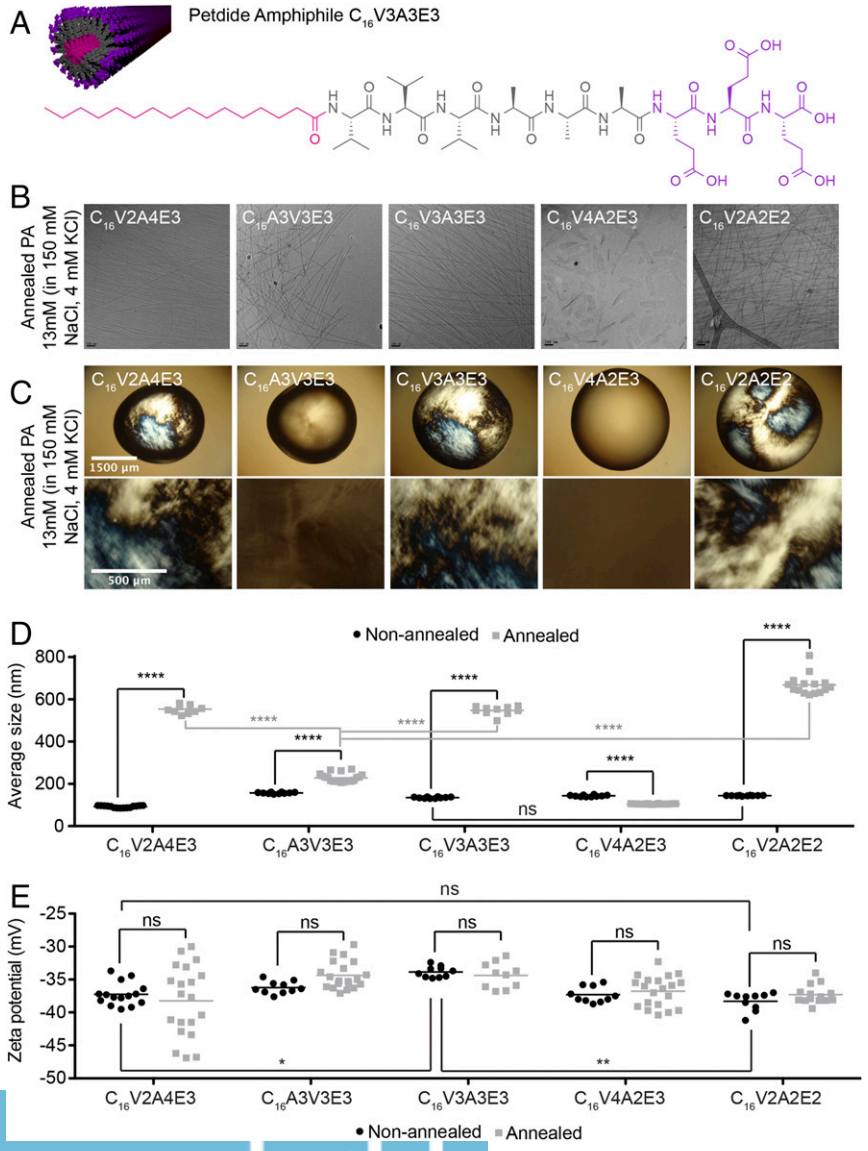

Fig. 1. Chemical and physical properties of peptide amphiphile solutions. (*A*) Chemical structure of a peptide amphiphile (PA) used to create scaffolds and molecular graphics representation of PA molecules - assembled into a supramolecular nanofiber. (*B*) Cryo transmission electron micrographs of different annealed 13-mM PA (aPA) solutions. (Scale bar, 100 nm.) (*C*) Birefringence images of different 13-mM aPA solutions. (Scale bars, 1,500 µm and 500 µm for the *Top* and *Bottom* images, respectively.) Average size (*D*) and zeta potential (*E*) measurements of annealed or nonannealed 0.13-mM PA solutions. The individual replicate measurements together with the mean (horizontal bar) are shown. $*P < 0.05$; $**P < 0.01$; $****P < 0.0001$; ns, nonsignificant; two-way ANOVA with Bonferroni post hoc test.

Downloaded at Palestinian Territory, occupied on December 4, 2021
www.manaraa.com

into self-sustaining "noodle"-shaped scaffolds. These gel scaffolds contained oriented or nonoriented nanofibers upon extrusion into or contact with another solution containing divalent ions, respectively, as previously described (25) (*SI Appendix*, Fig. S7*A*). These observations suggested that PA nanofiber length was a contributing factor to the liquid crystalline state of the solution. In fact nonannealed PA solutions, which are expected to contain shorter nanofibers (*SI Appendix*, Fig. S1), lacked birefringence except for C_{16}V3A3E3 (*SI Appendix*, Fig. S7*B*).

To characterize further changes in the nanoscale structure of fibers upon annealing, we performed dynamic light scattering (DLS) and zeta potential measurements on 0.13-mM solutions (Fig. 1 *D* and *E*). Since we found the nanostructures to be the same as their 13-mM counterparts (*SI Appendix*, Fig. S7*C*), we believe these measurements are indicative of nanostructure behavior at both concentrations. When fit to a protein-size model, the average size of the nanostructures, as measured by DLS, significantly increased for all PAs after annealing except for C_{16}V4A2E3, which decreased (Fig. 1*D*). In the case of C_{16}A3V3E3, even though the size increase was significant, it was also significantly lower than the other three aPAs (C_{16}V2A4E3, C_{16}V3A3E3, and C_{16}V2A2E2) (Fig. 1*D*). We then measured the zeta potential of these 0.13-mM PA solutions and found that nonannealed C_{16}V3A3E3 was significantly less negative than both C_{16}V2A4E3 and C_{16}V2A2E2 (Fig. 1*E*). The fact that nonannealed C_{16}V3A3E3 displayed birefringence (*SI Appendix*, Fig. S7*B*), but its DLS size was not different from C_{16}V2A2E2 (Fig. 1*D*), suggests that PA solutions containing short, negatively charged PA nanofibers might also display liquid crystalline behavior if their zeta potential is not "too" negative. Together, these results suggest that DLS and zeta potential measurements can be used to predict which PA solutions, annealed or not, will display liquid crystalline behavior. However, elucidating the exact contributions of each factor will require future studies and it is beyond the scope of this work.

Survival of Myogenic Progenitors Encapsulated in PA Scaffolds with Different Degrees of Stiffness. As described above, lyotropic liquid crystals formed by PA nanostructures and gelled by extruding a PA solution into another solution with divalent ions organize into a hierarchical structure of oriented nanofibers that partially emulates the architecture of macroscopically oriented muscle tissue (*SI Appendix*, Fig. S7*A*). We mixed C2C12-GFP mouse skeletal muscle progenitor cells (myoblasts) with aPA solutions and gelled them concomitantly to the application of a shear force by extrusion of the mixture through a pipette tip. We observed that these constructs contained oriented nanofibers, parallel to the direction of the applied shear force, and cells were uniformly distributed within and between nanofibers (Fig. 2*A*). These aPA/cell constructs also conserved most of their birefringence compared with their noncell-seeded counterparts, attesting to the maintenance of long-range oriented domains in the presence of cells (*SI Appendix*, Fig. S8). We then measured the stiffness of "bulk" gels generated by 13-mM aPA solutions and observed shear storage moduli (G′) spanning a range of two orders of magnitude, from 10^3 to 10^4 Pa (Fig. 2*B* and *SI Appendix*, Fig. S9*A*). Since the extruded constructs contain nanofibers oriented mostly in the same direction, cells embedded in those gels might experience anisotropic mechanics. Hence, we also performed atomic force microscopy (AFM) measurements to control for orientational artifacts on stiffness (Fig. 2*C* and *SI Appendix*, Fig. S9). We found that on oriented constructs, the Young's modulus (E) of each aPA gel closely resembled their bulk gel G′ counterpart, and they were all significantly different from each other depending on PA chemical structure (Fig. 2*C*). In nonoriented gels, however, the values of E were lower and did not follow the same trend as the E values on oriented gels or G′ values on bulk gels (*SI Appendix*, Fig. S9*B*). E measurements on nonoriented gels are technically challenging and difficult to interpret since the solutions from which they are formed already have domains of orientation that can be larger than the size scale of a cell (Fig. 1*C*), while the surface can have nanofibers with a random distribution of orientations (*SI Appendix*, Fig. S7*A*).

Given prior reports by us and others showing that MuSC and myoblast function is exquisitely sensitive to hydrogel substrate stiffness (21, 22, 26), we tested in vitro at different time points if gel stiffness had an effect on myogenic cell survival within oriented aPA/cell constructs. We examined low (~3 kPa), mid (~9 kPa), and high (~15 kPa) G′ aPAs and found that viability in all conditions was >85%, and both the mid G′ and the high G′ aPA scaffolds supported slightly higher cell viability than the low G′ (Fig. 2 *D* and *E*).

aPA Gel Nanofiber Alignment and Stiffness Direct the Alignment, Proliferation, and Maturation of Myogenic Progenitors. A number of natural (30) or synthetic (31, 32) biomaterials engendered with oriented fibrous structures can promote elongation, fusion, and differentiation of myoblasts that are seeded on top of them. For myoblasts embedded in randomly oriented natural (33) and synthetic (34) biomaterials, the application of passive force (or stretch) is necessary to promote the same effects. We hypothesized that the anisotropic nanofiber orientation within the aPA scaffolds, combined with their biomimetic stiffness (26), would serve as topological and mechanical cues to promote encapsulated myoblast alignment and differentiation, without additional applied forces.

To determine if aPA stiffness directed myoblast alignment, we fabricated aPA/cell constructs containing C2C12-GFP cells at 20,000 cells per microliter in oriented aPA scaffolds with low, mid, and high G′ or in nonoriented mid G′ aPA scaffolds. We then imaged the constructs after 2, 4, and 7 d in culture in low-serum differentiation media (DM) (Fig. 3*A*). Using a freely available plugin in Fiji we extracted a measure of alignment based on directionality analysis (*Materials and Methods* and Fig. 3*B*) that we termed "order parameter" (Fig. 3*C*). Compared with the nonoriented scaffold, the three oriented aPA scaffolds induced a higher degree of cell alignment and the mid and high G′ aPA scaffolds induced even greater alignment compared with the low G′ one at all days of culture (Fig. 3 *A* and *C*). This was more clearly visualized with confocal fluorescence stacks and scanning electron micrographs of C2C12-GFP cells in either oriented or nonoriented mid G′ aPA gels (*SI Appendix*, Fig. S10 and Movie S1). As cell alignment decreased by day 7 (Fig. 3*C*), we hypothesized that cell activity and growth led to increased aPA scaffold remodeling and decreased cell accessibility to the scaffold's oriented nanofibers. To test this hypothesis, we fabricated aligned mid G′ aPA/cell constructs containing different densities of C2C12-GFP cells and imaged them at days 1 and 4 (*SI Appendix*, Fig. S11*A*). As expected, the degree of cell alignment was inversely proportional to cell density at either day in culture, supporting our nanofiber accessibility hypothesis (*SI Appendix*, Fig. S11 *B–D*). We also observed that when low and mid G′ aPA/cell constructs (50,000 cells per microliter) were kept in growth media (GM) instead of DM, they were more extensively remodeled by the cells, and that some cells were able to escape from the aPA scaffold and attach to the underlying tissue culture plate (*SI Appendix*, Fig. S12), mirroring the behavior of muscle stem cells as they migrate away from their associated myofibers after isolation and culture (35). Given these observations, we used an intermediate loading density (20,000 cells per microliter) to optimally balance scaffold stability and total cell numbers for subsequent C2C12 differentiation experiments.

To determine if cell alignment and differentiation were correlated, we maintained the aPA/cell constructs in DM and stained them at day 10 in culture for myosin heavy chain (MHC) and sarcomeric alpha-actinin (ACTN) to identify mature myogenic cells. We observed MHC and ACTN expression in elongated cells often spanning several cell nuclei in the mid G′ and high G′ (ACTN not tested) oriented aPA scaffolds, suggesting that cell fusion, typical of myotube maturation, coincided with cell differentiation (Fig. 3*D*).

Downloaded at Palestinian Territory, occupied on December 4, 2021

www.manaraa.com

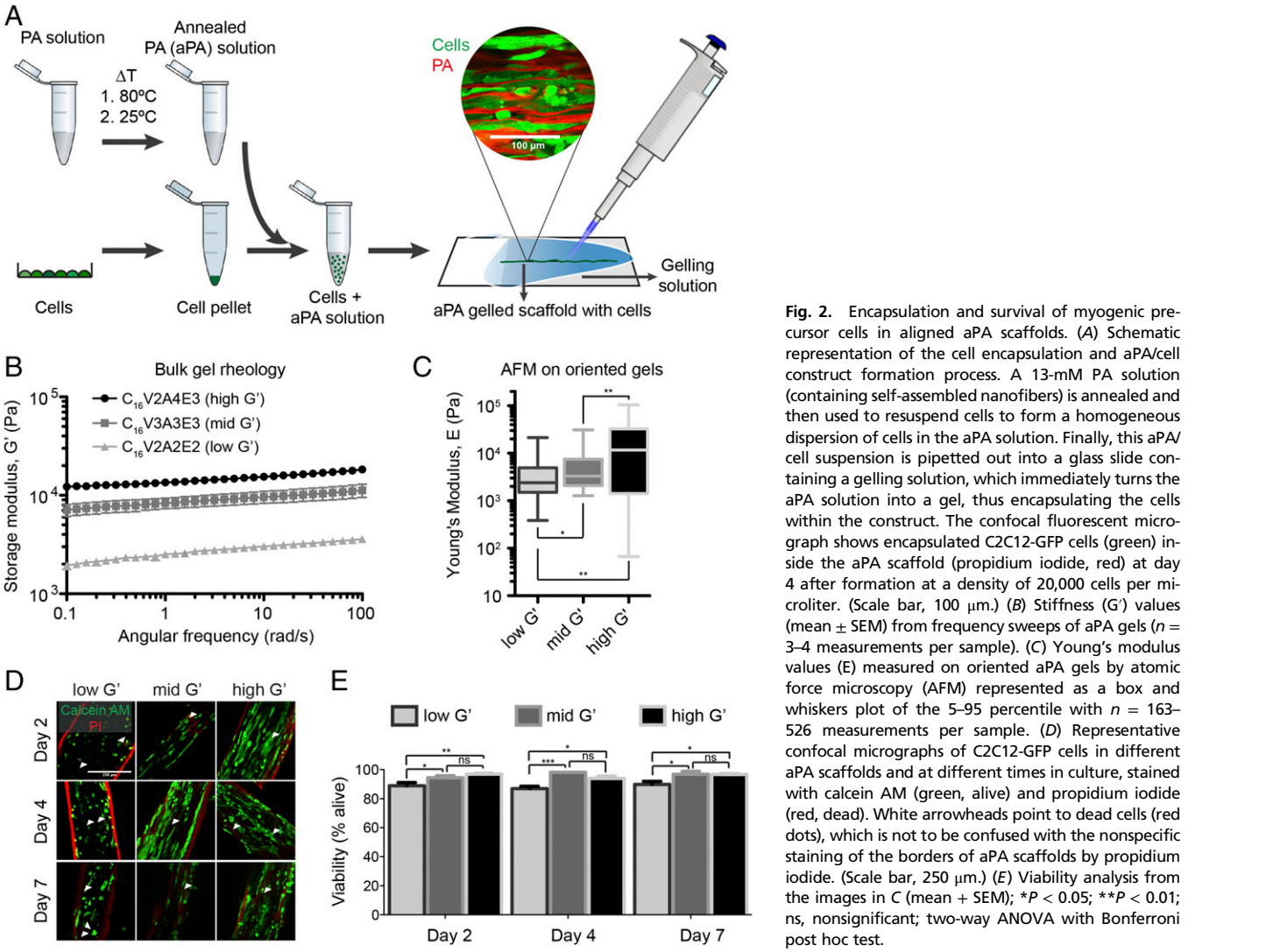

Fig. 2. Encapsulation and survival of myogenic precursor cells in aligned aPA scaffolds. (*A*) Schematic representation of the cell encapsulation and aPA/cell construct formation process. A 13-mM PA solution (containing self-assembled nanofibers) is annealed and then used to resuspend cells to form a homogeneous dispersion of cells in the aPA solution. Finally, this aPA/cell suspension is pipetted out into a glass slide containing a gelling solution, which immediately turns the aPA solution into a gel, thus encapsulating the cells within the construct. The confocal fluorescent micrograph shows encapsulated C2C12-GFP cells (green) inside the aPA scaffold (propidium iodide, red) at day 4 after formation at a density of 20,000 cells per microliter. (Scale bar, 100 μm.) (*B*) Stiffness (G′) values (mean ± SEM) from frequency sweeps of aPA gels (n = 3–4 measurements per sample). (*C*) Young's modulus values (E) measured on oriented aPA gels by atomic force microscopy (AFM) represented as a box and whiskers plot of the 5–95 percentile with n = 163–526 measurements per sample. (*D*) Representative confocal micrographs of C2C12-GFP cells in different aPA scaffolds and at different times in culture, stained with calcein AM (green, alive) and propidium iodide (red, dead). White arrowheads point to dead cells (red dots), which is not to be confused with the nonspecific staining of the borders of aPA scaffolds by propidium iodide. (Scale bar, 250 μm.) (*E*) Viability analysis from the images in *C* (mean + SEM); $*P < 0.05$; $**P < 0.01$; ns, nonsignificant; two-way ANOVA with Bonferroni post hoc test.

In nonoriented mid G′ and oriented low G′ aPA scaffolds, some cells stained positive for MHC, but they did not appear elongated or fused with each other, suggesting that both nanofiber orientation and gel stiffness are needed for these outcomes (Fig. 3*D*).

To assess C2C12-GFP proliferation in aPA scaffolds, we maintained aPA/cell constructs for 8 d in culture in DM and then counted the number of proliferating cells as measured by 24 h of EdU incorporation. We observed EdU^+ cells in all three oriented aPA/cell constructs but the frequency was highest in mid G′ and high G′ aPA scaffolds (Fig. 3*E*). Interestingly, we found cell proliferation to be significantly reduced in nonoriented mid G′ scaffolds (Fig. 3*D*). Overall, the oriented mid G′ and high G′ aPA scaffold demonstrated optimal structural and mechanical features for promoting myogenic cell proliferation and differentiation, but we selected the mid G′ aPA to further test its potency as a biomimetic scaffold for muscle cell transplantation therapy.

Development of an Injection Apparatus to Form Aligned Biomimetic Scaffolds in Vivo. PA solutions can be gelled in vivo by divalent ions within tissues. To maintain aPA nanofiber orientation upon injection and gelation in muscle tissues, we developed an injector apparatus by mounting a Hamilton microliter syringe to a linear moving platform. This apparatus allowed us to deliver small volumes of aPA/cell suspension mixture (less than 10 μL) with control of extrusion flow rate and retraction speed (Fig. 4 *A* and *B* and Movie S2). Using a 1-wt% agarose gel to model recipient tissue, we observed aPA nanofiber orientation parallel to the injection track when the needle's inner diameter matched the syringe's inner diameter (*Materials and Methods* and *SI Appendix*, Fig. S13). To monitor the localization of biomimetic scaffolds in vivo, we injected scaffolds mixed with Evans blue dye (EBD) or scaffolds containing 5 mol% of a PA molecule with a covalently attached gadolinium [Gd(III)] label (36, 37) (Fig. 4*H*) into the tibialis anterior (TA) muscles of C57BL/6 mice. The paramagnetic Gd(III) chelate produces positive contrast in magnetic resonance imaging (MRI), a technique providing unparalleled spatial resolution in vivo (38). After harvesting, we examined the tissues by macroscopic inspection or MRI of EBD-labeled or Gd(III)-labeled scaffolds. We found that biomimetic scaffolds were generated throughout the length of the recipient TA muscle and parallel to its long axis (Fig. 4 *C*, *D*, and *I*). To further assess the biomimetic scaffold's nanofiber orientation in vivo, we injected 1 μL of aPA solution into TA muscles and processed them for TEM. We observed that large domains within biomimetic scaffolds contained elongated nanofibers in parallel to the longitudinal direction of the neighboring endogenous tissue myofibers, thus confirming the generation of nanofiber orientation in vivo (Fig. 4 *E*–*G*).

Degradation Properties of Biomimetic Scaffolds in Vivo. Previous histological studies from our laboratory suggested that PA gels can remain in recipient tissues for up to a month (39, 40). Here, to track

Downloaded at Palestinian Territory, occupied on December 4, 2021
www.manaraa.com

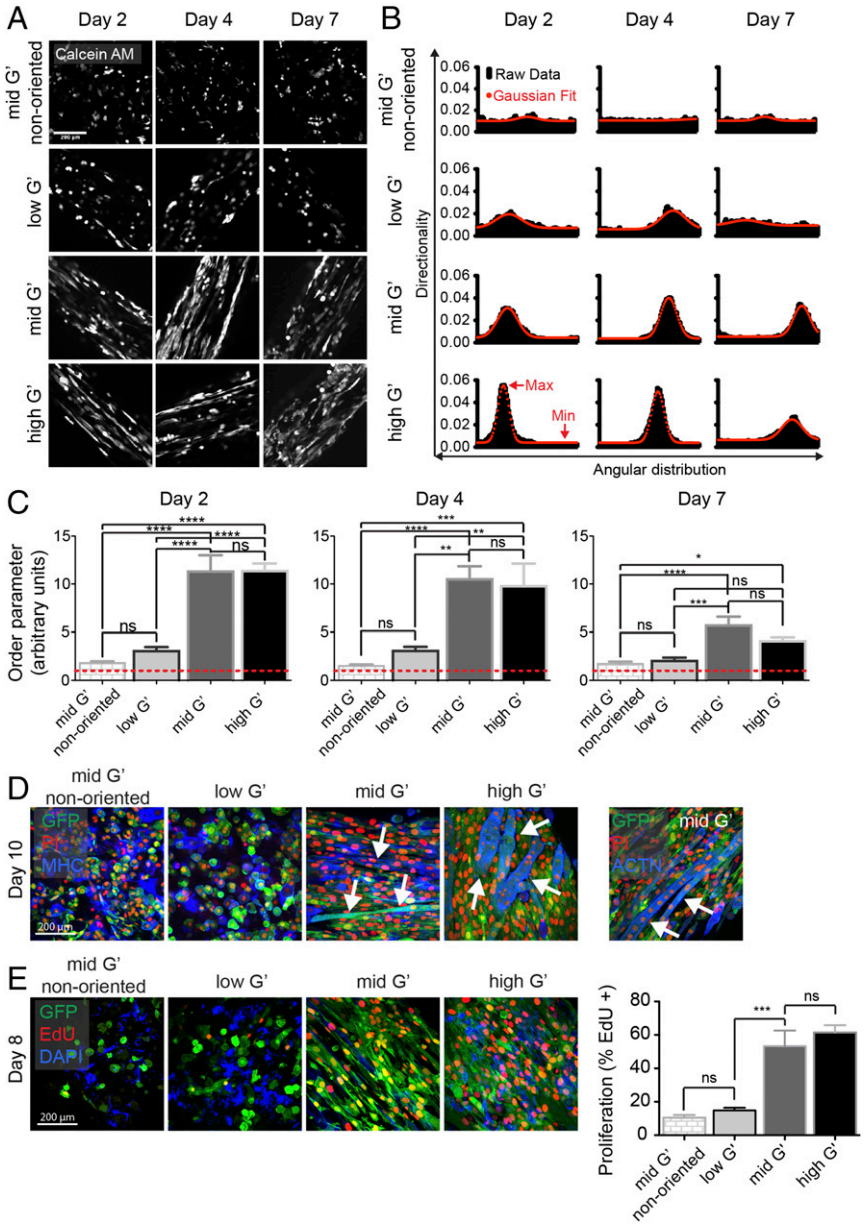

Fig. 3. aPA scaffold nanofiber alignment and stiffness modulate the alignment, maturation, and proliferation of C2C12-GFP cells. C2C12-GFPs were encapsulated at a density of 20,000 cells per microliter in nonaligned mid G′ aPA scaffolds or in aligned, aPA scaffolds with different stiffness magnitudes (low, mid, or high G′) and cultured for several days. (*A*) Representative confocal fluorescent micrographs of calcein AM-stained C2C12 cells in aPA scaffolds at different time points showing differential elongation of cells or cell clusters. (Scale bar, 200 μm.) (*B*) Directionality analysis from the images in *A*. The histograms show the angular distribution of the directions in which cells or cell clusters elongate (black bars) and the Gaussian equation that fits the data (red line). (*C*) As a measure of directionality, we divided the maximum by the minimum value of the Gaussian fit to calculate an order parameter (mean + SEM). When this order parameter is 1 (red dotted line), there is no preferred direction in the sample; greater values indicate greater directionality. $*P < 0.5$; $**P < 0.01$; $***P < 0.001$; $****P < 0.0001$; ns, nonsignificant; one-way ANOVA with Bonferroni post hoc test. (*D*) Representative confocal fluorescent micrographs of C2C12-GFP cells after 10 d in culture in aPA scaffolds displaying GFP (green) and stained for total nuclei (propidium iodide, red) and myosin heavy chain (MF20 antibody) or alpha-actinin,(ACTN) (blue). White arrows point to differentiated cells or cluster of cells that have likely fused with each other. (Scale bar, 200 μm.) (*E*, *Left*) Representative confocal micrographs of C2C12-GFP cells at day 8 in culture in aPA scaffolds displaying GFP (green) and stained for EdU incorporation (red) and total nuclei (DAPI, blue). (Scale bar, 250 μm.) (*Right*) Quantification of the percentage of cells that have incorporated EdU (24-h incubation), from the images above; $***P < 0.001$; ns, nonsignificant; one-way ANOVA with Bonferroni post hoc test.

and quantify the biomimetic scaffold's degradation in vivo over time, we made use of scaffolds containing the Gd(III) label (36) (Fig. 4*H*). In addition to MRI, the amount of Gd(III) label can also be quantified with great sensitivity using inductively coupled plasma mass spectrometry (ICP-MS) because of the negligible endogenous concentration of Gd(III) (41). Hence, we injected TA muscles of mice with Gd(III)-labeled scaffolds (Fig. 4*H*) and imaged them by MRI at 1, 4, 8, and 15 d (Fig. 4*I*). The Gd(III)-labeled scaffold was identifiable during the initial 8 d, but its signal approached background levels by day 15. Similar results were obtained after acquiring T_1 relaxation maps (*SI Appendix*, Fig. S14) and plotting the averaged T_1 values (Fig. 4*J*). To perform a more precise measurement of scaffold clearance from the tissue, we injected Gd(III)-labeled or nonlabeled scaffolds containing the same molar amount of unbound Gd(III) chelate (Prohance) and measured their Gd(III) content by ICP-MS at several time points up to 24 d (Fig. 4*K*). We

Downloaded at Palestinian Territory, occupied on December 4, 2021

www.manaraa.com

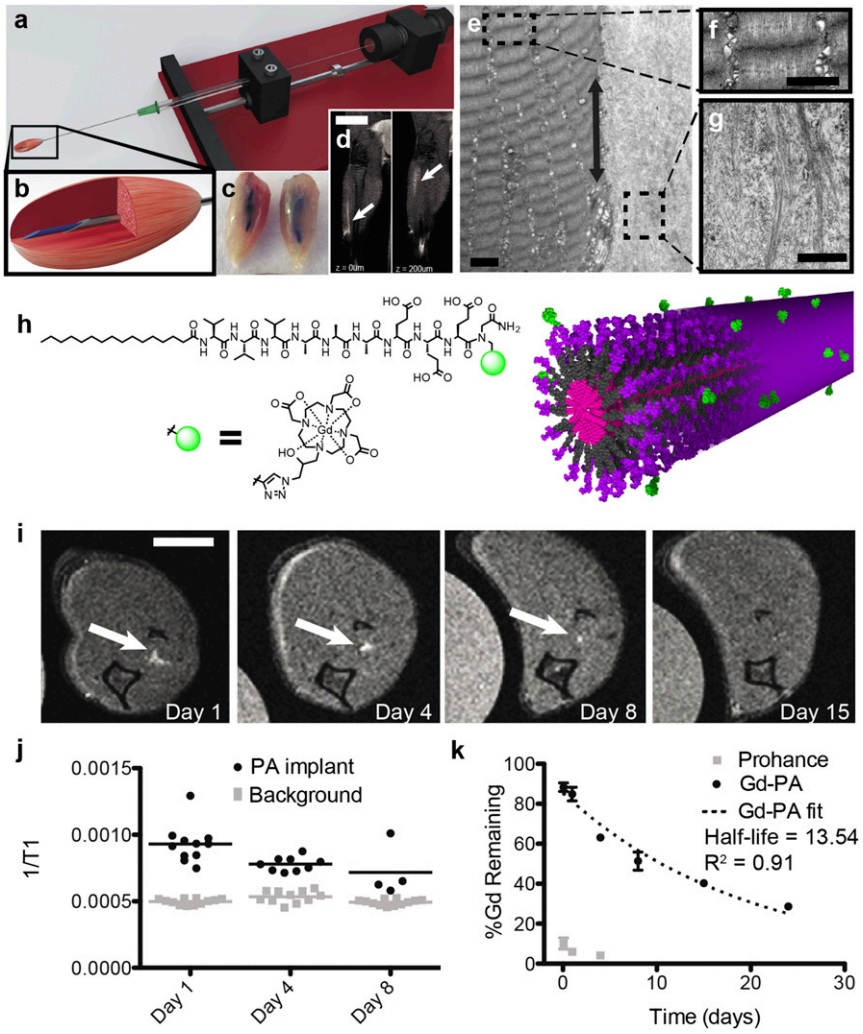

Fig. 4. Injector apparatus and its use with Gd(III)-labeled aPA to visualize and track aligned biomimetic scaffolds over time in vivo. (*A*) The injection device used for all injections is represented by this schematic showing a Hamilton syringe mounted onto a retracting leadscrew linear actuator platform. (*B*) The smaller zoomed *Inset* shows the aPA solution (blue) being injected into muscle tissue (Movie S2). (*C*) Macroscopic image of harvested TA muscles after injection with an Evans blue-dyed mid G′ aPA solution. (*D*) Two coronal MRI scans of the same mouse leg spaced 200 μm apart. The aPA scaffold can be seen throughout the length of the TA muscle (white arrows). (Scale bar, 1 cm.) (*E*) TEM showing TA muscle sarcomere banding next to injected aPA scaffold. The direction of the long axis of the muscle and of the aPA scaffold nanofibers are indicated by the black arrow. (*F* and *G*) Higher magnification *Insets* showing the muscle and the scaffold nanofibers, respectively; both the myofibers and nanofibers are oriented along the vertical direction parallel to the long axis of the muscle. (Scale bar, 1 μm.) (*H*) Molecular structure of the gadolinium chelate (green sphere) and PA molecule used for tracking the scaffold in vivo and molecular graphics of the supramolecular PA nanofiber composed of 5% Gd(III)-labeled PA and 95% C_{16}V3A3E3 PA. (*I*) Axial MRI scan showing the Gd-aPA scaffold (arrows) in the same leg for 8 d postinjection; the Gd-aPA is no longer distinguishable by day 15. (Scale bar, 500 μm.) (*J*) MRI signal quantified by T_1 relaxation time of the Gd-aPA area compared with the background muscle tissue (shown are the individual values as dots and the mean as a horizontal line). We were only able to discern the Gd-aPA signal from the background in fewer slices so the T_1 average at day 8 was most likely overestimated. (*K*) ICP-MS quantification of Gd(III) content in mice legs at different times postinjection (mean ± SEM). The one phase decay fit yields a half-life of 13.5 d for the scaffold.

found ∼85% of Gd(III) in the tissue 2 h after injection when the Gd(III)-labeled scaffold was used and decreased steadily over time to ∼30% by day 24. After fitting a one-phase decay equation to the data, we found that the Gd(III)-labeled scaffold's half-life in the TA muscle was 13.5 d, indicating that the scaffold is degrading during the time window of matrix remodeling typical of muscle regeneration (42). In contrast, we observed that the unbound chelate (Prohance) in the nonlabeled scaffolds was quickly cleared since Gd(III) was essentially absent by 2 h after injection (Fig. 4*K*), proving that ICP-MS measured the clearance of scaffold-bound Gd(III) and not free Gd(III) ion/chelate. It is interesting to note that while the Gd (III)-labeled scaffold was no longer identifiable at day 15 by MRI, the actual drop in Gd(III) content as measured by ICP-MS from day 8 to day 15 was only ∼10%. This suggests that either a portion of the Gd(III)-labeled scaffold diffused away from the injection site but remained in the muscle tissue for days before completely dissipating, or that there is still ∼40% of the scaffold in the injection site that cannot be observed by MRI due to a sensitivity limit in this configuration.

Encapsulation of Growth Factors by Biomimetic Scaffolds Enhances Primary Myoblast Proliferation in Vitro. We assessed the effects of the biomimetic scaffold on primary mouse myoblast encapsulation and transplantation. Primary myoblasts were ∼100% viable in biomimetic scaffolds when cultured in GM for 5 d but their viability decreased to ∼90% after switching to DM (*SI Appendix*, Fig. S15), suggesting that their survival is sensitive to growth factors (GFs) in the media. Moreover, we found that myoblasts in GM were highly proliferative at day 1 (∼90%) but that proliferation decreased over

Downloaded at Palestinian Territory, occupied on December 4, 2021
www.manaraa.com

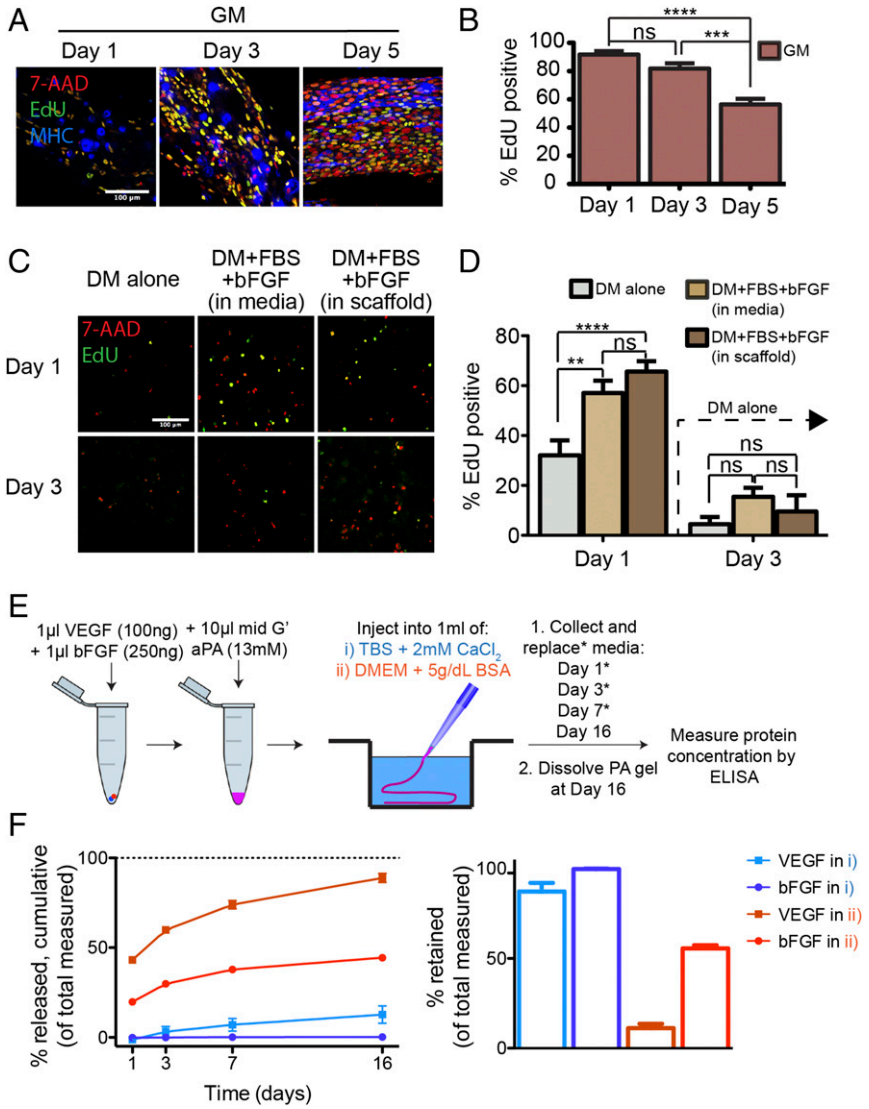

Fig. 5. Proliferation and differentiation of primary myoblasts in aPA scaffolds and GF encapsulation and release by aPA scaffolds in vitro. Primary myoblasts were encapsulated at a density of 10,000 cells per microliter. (*A* and *C*) Representative confocal micrographs of primary myoblasts in the mid G′ aPA scaffold at different time point culture conditions. Proliferating cells were stained for EdU incorporation (green) and total nuclei were stained with 7-AAD (red). Myosin heavy chain was stained using the MF20 antibody (*A*, blue). (Scale bar, 100 μm.) (*B* and *D*) Graph showing the quantification of EdU incorporation (24-h incubation), from the images in *A* and *C* (mean + SEM). (*C* and *D*) After the first day in culture, all media were changed to DM alone. $^{**}P < 0.01$; $^{***}P < 0.001$; $^{****}P < 0.0001$; ns, nonsignificant; one (*D*) or two-way (*B*) ANOVA with Bonferroni post hoc test. (*E*) Schematic representation of the protein encapsulation and release experiment. (*F*) Cumulative release (*Left*), and amount retained (*Right*), of VEGF and bFGF from mid G′ aPA gels in two different media, expressed as percentage of total (released + retained) (mean ± SEM).

time, reaching <60% at day 5 (Fig. 5 *A* and *B*). This decrease appeared to be correlated with increased differentiation, as evidenced by MHC immunostaining (Fig. 5*A*), resembling the in vivo myogenic regenerative progression (1). We hypothesized that the encapsulation of GFs within biomimetic scaffolds could enhance primary myoblast proliferation and engraftment in environments with low serum GFs. We first tested this possibility in vitro by culturing myoblasts in biomimetic scaffolds using DM alone, DM with FBS, and basic fibroblast growth factor (bFGF) in the media, or DM with FBS and bFGF contained in the aPA scaffold. By EdU staining (Fig. 5*C*) we observed that the encapsulation of GFs (FBS and bFGF) (43, 44) significantly increased the frequency of proliferating primary myoblasts (>60%) compared with DM alone (~30%), but had similar effects to GFs in the media after 1 d in culture (Fig. 5*D*). We then changed all media to DM alone and observed that proliferation dropped in all groups at day 3 (Fig. 5*D*). These results suggested that encapsulated GFs were active on primary myoblasts but that they also diffused into the surrounding media.

To further investigate the dynamics of protein retention and release in aPA gels, we encapsulated 100 ng of vascular endothelial growth factor (VEGF) and 250 ng of bFGF in 10 μL of mid G′ aPA solution and injected the resulting mixture into 1 mL of two different media (Fig. 5*E*). We then collected and replaced these media and tested both VEGF and bFGF release and retention by ELISA in the media and inside the gel, respectively (Fig. 5*E*). We found that both VEGF and bFGF were exceptionally well retained in media that did not contain protein over the course of 16 d (*i*) and that most of VEGF and bFGF were found inside the aPA gel (Fig. 5*F*). However, we observed significant release of both VEGF and bFGF in media that contained 5 g/dL of the "competing" protein BSA over the course of 16 d (*ii*) (Fig. 5*F*). This concentration of BSA is equal to that of the total

Downloaded at Palestinian Territory, occupied on December 4, 2021
www.manaraa.com

amount of serum protein found in common mouse strains, such as C57BL/6 (45). Hence, these results suggested that the mid G′ aPA gels would be able to retain and release GFs over the course of tissue regeneration in physiological conditions.

Biomimetic Scaffolds Loaded with GFs Enhance Engraftment of Transplanted MuSCs. We evaluated whether biomimetic scaffolds improved MuSC transplantation therapy using a transgenic transplantation model. Primary MuSCs were isolated by fluorescence-activated cell sorting (FACS) (3, 22) from digested hindlimbs of young adult Gfp/Luciferase double-transgenic mice. Luciferase-expressing MuSCs were injected intramuscularly (in a 1-μL volume) into preirradiated immunodeficient NOD/Scid recipients and followed dynamically by noninvasive bioluminescence imaging (BLI), a sensitive quantitative measure of cell engraftment after transplantation (3, 21, 22) (Fig. 6*A*). We compared biomimetic scaffolds formed with a myogenic GF mixture (bFGF + FBS) and with or without DMSO, a common carrier used for drug suspension studies. We observed no statistically significant effects of including DMSO so samples were grouped (Fig. 6 *B*–*D*). We transplanted a low number (200 cells) of MuSCs per injection, to enable discrimination between injection methods. This number of cells typically results in variable engraftment as reported previously (3), but when delivered with a biomimetic scaffold, the variability was greatly reduced and overall engraftment success was substantially improved, attesting to its beneficial effects (Fig. 6 *B*–*D*).

In uninjured recipients, GF-laden biomimetic scaffolds substantially enhanced MuSC engraftment and donor-cell-mediated myofiber repair posttransplant, due to expedited expansion within 2 wk (Fig. 6*B*) and a more frequent successful engraftment outcome at 5 wk (Fig. 6 *C* and *D*). Immunohistochemical analysis of donor (GFP^+)-derived cells showed enhanced transplanted cell contributions to mature myofibers at the completion of the repair process by MuSCs encapsulated in GF-laden biomimetic scaffolds compared with cells injected in buffer/GF mix (Fig. 6 *E* and *F*).

We observed a similar engraftment improvement in primary myoblast (progenitor) transplants. Primary myoblasts were derived from Gfp/Luc mice following culture and expansion and were injected in GF-laden biomimetic scaffolds. We transplanted 3,000 myoblasts, a cell number that results in infrequent engraftment owing to posttransplant myoblast death and differentiation (3, 22) (*SI Appendix*, Fig. S16*A*). Relative to buffer controls, we observed enhanced myoblast engraftment and proliferation in transplants with the aPA scaffold (*SI Appendix*, Fig. S16 *B*–*D*). The scaffolds improved myoblast survival as seen by comparing the fraction of transplants with detectable engraftment at 5 wk posttransplant (*SI*

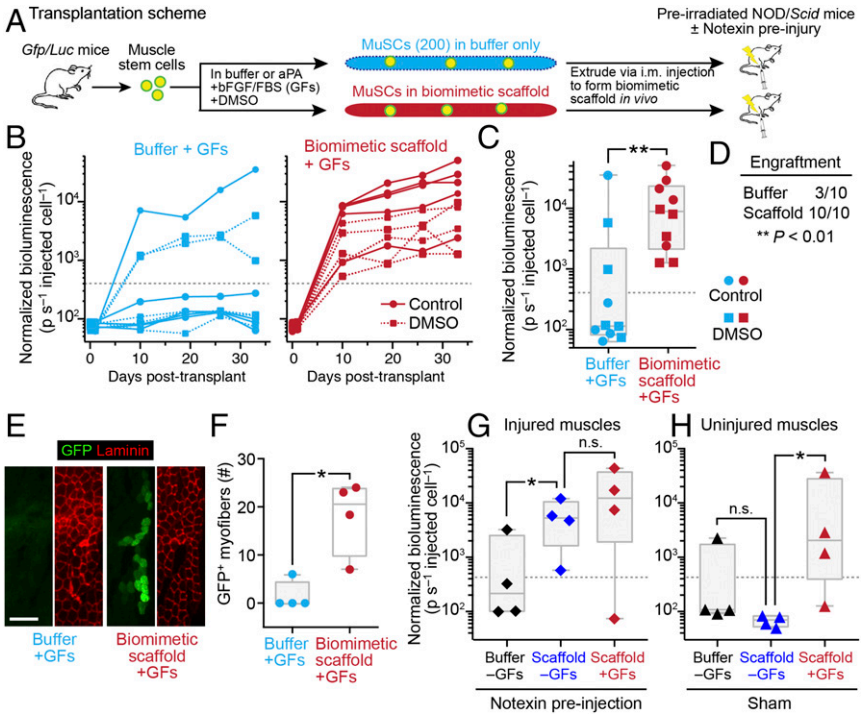

Fig. 6. Biomimetic scaffolds enhance MuSC transplantation therapy. (*A*) Primary mouse muscle stem cells were isolated from Gfp/Luciferase double-transgenic mice by $GFP^+/CD34^+/integrin\text{-}\alpha_7^+$ FACS sorting and mixed with 13 mM mid G′ aPA solution containing bFGF and FBS ("+GF") or no serum/growth factors ("−GFs"; in *G* and *H* only) at 200 cells μL^{-1}. Biomimetic scaffold/MuSC mixtures (1 μL per muscle) were extruded into the TA muscles of preirradiated NOD/Scid by intramuscular injection to form biomimetic scaffolds in situ. In contralateral hindlimbs, control MuSC injections were performed in resuspension buffer ±GFs. Injections were performed with or without DMSO (1.8% final) to evaluate the effect of carrier in drug resuspension studies. No statistically significant effects between control (DMSO-free) and DMSO condition were observed for any comparison so $n = 10$ samples were grouped per method. Some hindlimbs were injured by intramuscular injection of notexin 3 d pretransplant in *G*. (*B*–*F*) BLI and immunohistochemical detection transplanted MuSC engraftment and myofiber repair in uninjured muscles. Engraftment threshold (dashed line) corresponding to histological detection of one or more donor-derived (GFP^+) myofibers (as in refs. 21 and 22). (*B*) BLI normalized to injected cell number at 0–5 wk posttransplant of $n = 10$ total (five control, five DMSO) transplants grouped by injection method (p, photons). $^{***}P < 0.0001$ by two-way ANOVA with Bonferroni post hoc test for comparison of time courses. (*C*) Normalized BLI values at 5 wk posttransplant. Scatterplot overlain on box (50%) and whisker (full range) with median line. $^{**}P < 0.01$ by Mann–Whitney *U* test on confidence intervals of endpoints. (*D*) Engraftment analysis using threshold BLI value. $^{**}P < 0.01$ by Fisher's test on endpoint values. (*E* and *F*) Detection of transplant-derived (GFP^+) myofibers by anti-GFP and anti-laminin immunohistochemistry from DMSO-free transplants. (*E*) Representative immunohistological images. (Scale bar, 500 μm.) (*F*) GFP^+ myofibers per recipient TA muscle (median line). $n = 4$ transplants per method. (*G* and *H*) BLI detection (5 wk posttransplant) of MuSC engraftment into either uninjured (*H*) or notexin preinjured hindlimb muscles (*G*) via biomimetic scaffold encapsulation, with and without bFGF/FBS-loading but not DMSO. Scatterplot shows $n = 4$ transplants per condition with median line. In *F*–*H*, $^{*}P < 0.05$ by Mann–Whitney *U* test. ns, not significant.

Downloaded at Palestinian Territory, occupied on December 4, 2021
www.manaraa.com

Appendix, Fig. S16*D*). Importantly, myoblast transplantation was successful with GF-laden biomimetic scaffolds even in the absence of chemically or mechanically induced muscle injury, which is often used to enhance the regenerative function of transplanted myogenic cells (3, 6, 17, 22).

To more closely examine the effects of muscle injury, we performed MuSC transplants into recipient muscles previously injured with the snake venom toxin notexin, a standard injury paradigm that induces extensive damage throughout the injected muscle, together with scaffolds with and without GFs (Fig. 6*G*). Notably, in injured muscles, the GF inclusions were not required as the GF-free scaffolds markedly improved MuSC engraftment compared with buffer (−GF) controls (Fig. 6*G*). We hypothesized that injured muscles may transiently generate sufficient prosurvival signals from infiltrating macrophages (46–50) that act in synergy with the GF-free scaffolds, enhancing MuSC engraftment. Hence, we reasoned that GFs codelivered within aPA scaffolds might improve MuSC engraftment and overcome the need for notexin injury in the standard injection paradigm, allowing for a minimal injury approach more favorable to clinical application (Fig. 6*H*). We observed that, in contrast to MuSC delivery with buffer or scaffold alone, in which cells did not engraft, the GF mixture was required for the marked scaffold-enhanced MuSC transplant engraftment in uninjured recipients (Fig. 6*H*). Taken together, our observations demonstrate that the biomimetic scaffold system enhances engraftment of muscle stem and progenitor cells, and, in conjunction with GFs, can augment their proliferation, differentiation, and function in muscle repair posttransplantation.

Discussion

The discovery of murine MuSCs capable of robustly regenerating and restoring strength to injured muscles (1, 3, 7, 16–19), and a means for their expansion in culture using inducers such as p38 MAPK inhibitors, has provided a framework for their future clinical application (22, 51–53). Moreover, recent strides in the isolation and characterization of their human counterparts from tissues or as derivatives from human embryonic stem (ES) or induced pluripotent stem (iPS) cells (54–59) now facilitate the use of these potent cell types as a muscle cell therapeutic. Nonetheless, efficient cell delivery remains a hurdle to translation.

To overcome this hurdle, we developed an injectable muscle cell delivery scaffold based on PA nanofibers that gels in vitro and in vivo into a matrix of macroscopically aligned and bundled fibers with the use of minimal shear force. This property is a direct result of the lyotropic liquid crystalline nature of the supramolecular nanofibers used to create the scaffold. We have shown here that this liquid crystalline nature correlates with certain physical properties of the PA solution, that is, its zeta potential and the size of PA nanofibers. This is important since any newly developed PA can now be tested using these techniques to learn their propensity to form liquid crystalline solutions and scaffolds. We have also shown that these 3D biomimetic scaffolds that model the macroscopically oriented microarchitecture of extracellular matrix components in muscle (60) are highly effective environments for the culture and transplantation of muscle stem and progenitor cells. This biomimetic structure provides a substrate with a stiffness that closely mimics the elasticity of skeletal muscle (~5–40 kPa elastic modulus) (21, 22, 26). It supports myogenic cell viability and proliferation, as well as alignment and maturation in vitro and proliferation and fusion of grafted cells into endogenous myofibers of muscle tissues in vivo. It is interesting to note that the extracellular matrix remnants from injured skeletal muscle fibers ("ghost fibers") govern several aspects of muscle stem/progenitor cell behavior, including the direction of cell division and migration, in vivo (61). Thus, our biomimetic scaffolds may mirror the regenerative role of native ghost fiber scaffolds. The strong liquid crystallinity and therefore shear sensitivity of the scaffold makes it virtually impossible to create a nonoriented control scaffold. However, based on the previous ghost fiber observations, and our in vitro work on cell alignment, proliferation, and differentiation in the gelled liquid crystalline scaffold, we hypothesize that macroscopic alignment is beneficial to cell engraftment.

The biomimetic scaffold offers several critical advantages for therapeutic translation. Compared with decellularized muscle (62), other natural biomaterials (63, 64), or natural/synthetic composites (65), our all-synthetic biomimetic scaffolds allow the transplantation of muscle stem and progenitor cells in a chemically defined environment. Moreover, their neutral pH and instantaneous gelation upon injection in vivo make our biomimetic scaffolds ideal for cell transplantation. Its degradation kinetics in vivo (~14 d), which approximate that of normal regeneration (42), allow for cell protection and enhanced viability at the onset. We hypothesize that this feature will also enable subsequent innervation and angiogenesis critical to long-term muscle function, but further experiments are needed to confirm this effect. These aPA scaffolds can be laden with protein growth factors to further enhance survival and expansion of MuSCs after delivery into either healthy or damaged muscle tissues further facilitating clinical translation. We believe that the scaffold's ability to bind and retain proteins also plays a role in allowing cell attachment to the scaffold's nanofibers since they do not contain cell-binding epitopes such as RGD (66). We also hypothesize that other sources of muscle stem and progenitor cells, including those obtained from embryonic and induced pluripotent stem cells (56–59), could benefit from transplantation with these biomimetic scaffolds. Lastly, the controlled pump delivery method for the biomimetic scaffold is simple, yet critical to the achievement of long-range alignment of the nanofibers (*Materials and Methods*). There are challenges in directly comparing our data with others due to differences in injected cell numbers, injury model, presence or absence of scaffold, the type of scaffold due to mode of gelation or cross-linking, and mode of injection (67). However, the biomimetic scaffolds described here constitute a broadly applicable stem cell delivery technology with the potential to substantially impact regenerative medicine.

Materials and Methods

We generated PAs consisting of an aliphatic (C_{16}) palmitoyl tail and a hydrophilic six or nine amino acid cap using a custom peptide synthesizer. We annealed PAs into randomly ordered, long-axis nanofibers, which externally expose the amino acid cap and internally aggregate the hydrophobic tail, by entropic mixing. We extruded aPAs into physiological calcium concentrations in culture medium to fabricate a stable, noodle-like aPA scaffolds with liquid crystalline properties due to their highly ordered nanofibers in parallel to the direction of extrusion. We measured the storage modulus of aPA scaffolds using shear rheometry and AFM. We evaluated myogenic progenitor cell viability, proliferation, and differentiation after encapsulation in assembled aPA scaffolds in vitro in growth and differentiation media. We transplanted FACS-isolated α7-integrin$^+$ CD34$^+$ muscle stem cells from GFP/Luciferase transgenic mice mixed with a 13-mM aPA solution by rate-controlled injection into hindlimb muscles of irradiated immunodeficient NOD/scid mice and measured muscle repair by bioluminescence imaging and anti-GFP immunohistochemistry at 1-mo posttransplant. aPA scaffold degradation in vivo was assayed using Gd(III)-doped PA molecules and MRI imaging and ICP analysis every 5 d. Please refer to *SI Appendix* for details.

ACKNOWLEDGMENTS. We thank Kassie Koleckar, Peggy Kraft, John Ramunas, Steven Lee, and Feng Chen for technical assistance; Nicholas Stephanopolous for insightful discussions on the biomaterials used in this work; and Emily Alex Waters and Chad R. Haney for their help with MRI. We also acknowledge Northwestern University's Peptide Core and Equipment Core at the Simpson Querrey Institute of BioNanotechnology, the Stanford Center for Innovation in In-Vivo Imaging (SCI3), and the Stanford Shared FACS Facility for core facility support. Imaging work was performed at the Northwestern University Center for Advanced Microscopy, and the Center for Advanced Molecular Imaging generously supported by National Cancer Institute Cancer Center Support Grant P30 CA060553 awarded to the Robert H. Lurie Comprehensive Cancer Center. This work also made use of the Scanned Probe Imaging and Development facility of the NUANCE Center at Northwestern University, which has received support from the Soft and Hybrid Nanotechnology Experimental

PNAS PLUS
APPLIED BIOLOGICAL SCIENCES
Downloaded at Palestinian Territory, occupied on December 4, 2021
www.manaraa.com

Resource [National Science Foundation (NSF) NNCI-1542205]; the Materials Research Science and Engineering Centers program (NSF DMR-1121262) at the Materials Research Center; the International Institute for Nanotechnology (IIN); the Keck Foundation; and the State of Illinois, through the IIN. At Northwestern University this work was supported by the NIH through National Heart, Lung, and Blood Institute (NHLBI) PPG Grant 1P01HL108795, the NIH/NHLBI Bioengineering Research Partnership Grant (5R01HL116577), and the Louis A. Simpson and Kimberly K. Querrey Center for Regenerative Nanomedicine. At Stanford University, this work was supported by the Baxter Foundation, California Institute for Regenerative Medicine Grant RB5-07469, and NIH Grant AG020961 (to H.M.B.) and K99AG042491 (to B.D.C.). At Cornell University, this work was supported by NIH Grant R00AG042491 (to B.D.C.).

1. Tedesco FS, Dellavalle A, Diaz-Manera J, Messina G, Cossu G (2010) Repairing skeletal muscle: Regenerative potential of skeletal muscle stem cells. *J Clin Invest* 120:11–19.
2. Mauro A (1961) Satellite cell of skeletal muscle fibers. *J Biophys Biochem Cytol* 9: 493–495.
3. Sacco A, Doyonnas R, Kraft P, Vitorovic S, Blau HM (2008) Self-renewal and expansion of single transplanted muscle stem cells. *Nature* 456:502–506.
4. Brack AS, Rando TA (2012) Tissue-specific stem cells: Lessons from the skeletal muscle satellite cell. *Cell Stem Cell* 10:504–514.
5. Lepper C, Partridge TA, Fan C-M (2011) An absolute requirement for Pax7-positive satellite cells in acute injury-induced skeletal muscle regeneration. *Development* 138: 3639–3646.
6. Collins CA, et al. (2005) Stem cell function, self-renewal, and behavioral heterogeneity of cells from the adult muscle satellite cell niche. *Cell* 122:289–301.
7. Montarras D, et al. (2005) Direct isolation of satellite cells for skeletal muscle regeneration. *Science* 309:2064–2067.
8. Günther S, et al. (2013) Myf5-positive satellite cells contribute to Pax7-dependent long-term maintenance of adult muscle stem cells. *Cell Stem Cell* 13:590–601.
9. Sambasivan R, et al. (2011) Pax7-expressing satellite cells are indispensable for adult skeletal muscle regeneration. *Development* 138:3647–3656.
10. von Maltzahn J, Jones AE, Parks RJ, Rudnicki MA (2013) Pax7 is critical for the normal function of satellite cells in adult skeletal muscle. *Proc Natl Acad Sci USA* 110: 16474–16479.
11. Partridge TA, Morgan JE, Coulton GR, Hoffman EP, Kunkel LM (1989) Conversion of mdx myofibres from dystrophin-negative to -positive by injection of normal myoblasts. *Nature* 337:176–179.
12. Briggs D, Morgan JE (2013) Recent progress in satellite cell/myoblast engraftment: Relevance for therapy. *FEBS J* 280:4281–4293.
13. Gussoni E, et al. (1992) Normal dystrophin transcripts detected in Duchenne muscular dystrophy patients after myoblast transplantation. *Nature* 356:435–438.
14. Gussoni E, Blau HM, Kunkel LM (1997) The fate of individual myoblasts after transplantation into muscles of DMD patients. *Nat Med* 3:970–977.
15. Skuk D, Tremblay JP (2011) Intramuscular cell transplantation as a potential treatment of myopathies: Clinical and preclinical relevant data. *Expert Opin Biol Ther* 11: 359–374.
16. Bosnakovski D, et al. (2008) Prospective isolation of skeletal muscle stem cells with a Pax7 reporter. *Stem Cells* 26:3194–3204.
17. Cerletti M, et al. (2008) Highly efficient, functional engraftment of skeletal muscle stem cells in dystrophic muscles. *Cell* 134:37–47.
18. Tanaka KK, et al. (2009) Syndecan-4-expressing muscle progenitor cells in the SP engraft as satellite cells during muscle regeneration. *Cell Stem Cell* 4:217–225.
19. Kuang S, Kuroda K, Le Grand F, Rudnicki MA (2007) Asymmetric self-renewal and commitment of satellite stem cells in muscle. *Cell* 129:999–1010.
20. Cosgrove BD, Sacco A, Gilbert PM, Blau HM (2009) A home away from home: Challenges and opportunities in engineering in vitro muscle satellite cell niches. *Differentiation* 78:185–194.
21. Gilbert PM, et al. (2010) Substrate elasticity regulates skeletal muscle stem cell self-renewal in culture. *Science* 329:1078–1081.
22. Cosgrove BD, et al. (2014) Rejuvenation of the muscle stem cell population restores strength to injured aged muscles. *Nat Med* 20:255–264.
23. Qazi TH, Mooney DJ, Pumberger M, Geissler S, Duda GN (2015) Biomaterials based strategies for skeletal muscle tissue engineering: Existing technologies and future trends. *Biomaterials* 53:502–521.
24. Juhas M, Ye J, Bursac N (2016) Design, evaluation, and application of engineered skeletal muscle. *Methods* 99:81–90.
25. Zhang S, et al. (2010) A self-assembly pathway to aligned monodomain gels. *Nat Mater* 9:594–601.
26. Engler AJ, et al. (2004) Myotubes differentiate optimally on substrates with tissue-like stiffness: Pathological implications for soft or stiff microenvironments. *J Cell Biol* 166: 877–887.
27. Hartgerink JD, Beniash E, Stupp SI (2001) Self-assembly and mineralization of peptide-amphiphile nanofibers. *Science* 294:1684–1688.
28. Tantakitti F, et al. (2016) Energy landscapes and functions of supramolecular systems. *Nat Mater* 15:469–476.
29. Pashuck ET, Cui H, Stupp SI (2010) Tuning supramolecular rigidity of peptide fibers through molecular structure. *J Am Chem Soc* 132:6041–6046.
30. Yan W, et al. (2007) Tissue engineering of skeletal muscle. *Tissue Eng* 13:2781–2790.
31. Ku SH, Lee SH, Park CB (2012) Synergic effects of nanofiber alignment and electroactivity on myoblast differentiation. *Biomaterials* 33:6098–6104.
32. Wang L, Wu Y, Guo B, Ma PX (2015) Nanofiber yarn/hydrogel core-shell scaffolds mimicking native skeletal muscle tissue for guiding 3D myoblast alignment, elongation, and differentiation. *ACS Nano* 9:9167–9179.
33. Hinds S, Bian W, Dennis RG, Bursac N (2011) The role of extracellular matrix composition in structure and function of bioengineered skeletal muscle. *Biomaterials* 32: 3575–3583.
34. Li Y, et al. (2015) Chinese-noodle-inspired muscle myofiber fabrication. *Adv Funct Mater* 25:5999–6008.
35. Bischoff R (1975) Regeneration of single skeletal muscle fibers in vitro. *Anat Rec* 182: 215–235.
36. Preslar AT, et al. (2014) Gd(III)-labeled peptide nanofibers for reporting on biomaterial localization in vivo. *ACS Nano* 8:7325–7332.
37. Bull SR, et al. (2005) Magnetic resonance imaging of self-assembled biomaterial scaffolds. *Bioconjug Chem* 16:1343–1348.
38. Heffern MC, Matosziuk LM, Meade TJ (2014) Lanthanide probes for bioresponsive imaging. *Chem Rev* 114:4496–4539.
39. Webber MJ, et al. (2011) Supramolecular nanostructures that mimic VEGF as a strategy for ischemic tissue repair. *Proc Natl Acad Sci USA* 108:13438–13443.
40. Ghanaati S, et al. (2011) Evaluation of the tissue reaction to a new bilayered collagen matrix in vivo and its translation to the clinic. *Biomed Mater* 6:015010.
41. Harrison VS, Carney CE, MacRenaris KW, Waters EA, Meade TJ (2015) Multimeric near IR-MR contrast agent for multimodal in vivo imaging. *J Am Chem Soc* 137:9108–9116.
42. Murphy MM, Lawson JA, Mathew SJ, Hutcheson DA, Kardon G (2011) Satellite cells, connective tissue fibroblasts and their interactions are crucial for muscle regeneration. *Development* 138:3625–3637.
43. Rando TA, Blau HM (1994) Primary mouse myoblast purification, characterization, and transplantation for cell-mediated gene therapy. *J Cell Biol* 125:1275–1287.
44. Bischoff R (1986) Proliferation of muscle satellite cells on intact myofibers in culture. *Dev Biol* 115:129–139.
45. Zaias J, Mineau M, Cray C, Yoon D, Altman NH (2009) Reference values for serum proteins of common laboratory rodent strains. *J Am Assoc Lab Anim Sci* 48:387–390.
46. Chazaud B (2016) Inflammation during skeletal muscle regeneration and tissue remodeling: Application to exercise-induced muscle damage management. *Immunol Cell Biol* 94:140–145.
47. Lescaudron L, et al. (1999) Blood borne macrophages are essential for the triggering of muscle regeneration following muscle transplant. *Neuromuscul Disord* 9:72–80.
48. Lluís F, et al. (2001) Urokinase-dependent plasminogen activation is required for efficient skeletal muscle regeneration in vivo. *Blood* 97:1703–1711.
49. Godwin JW, Pinto AR, Rosenthal NA (2013) Macrophages are required for adult salamander limb regeneration. *Proc Natl Acad Sci USA* 110:9415–9420.
50. Merly F, Lescaudron L, Rouaud T, Crossin F, Gardahaut MF (1999) Macrophages enhance muscle satellite cell proliferation and delay their differentiation. *Muscle Nerve* 22:724–732.
51. Bernet JD, et al. (2014) p38 MAPK signaling underlies a cell-autonomous loss of stem cell self-renewal in skeletal muscle of aged mice. *Nat Med* 20:265–271.
52. Price FD, et al. (2014) Inhibition of JAK-STAT signaling stimulates adult satellite cell function. *Nat Med* 20:1174–1181.
53. Tierney MT, et al. (2014) STAT3 signaling controls satellite cell expansion and skeletal muscle repair. *Nat Med* 20:1182–1186.
54. Charville GW, et al. (2015) Ex vivo expansion and in vivo self-renewal of human muscle stem cells. *Stem Cell Rep* 5:621–632.
55. Xu X, et al. (2015) Human satellite cell transplantation and regeneration from diverse skeletal muscles. *Stem Cell Rep* 5:419–434.
56. Chal J, et al. (2015) Differentiation of pluripotent stem cells to muscle fiber to model Duchenne muscular dystrophy. *Nat Biotechnol* 33:962–969.
57. Tedesco FS, et al. (2012) Transplantation of genetically corrected human iPSC-derived progenitors in mice with limb-girdle muscular dystrophy. *Sci Transl Med* 4:140ra89.
58. Rinaldi F, Perlingeiro RCR (2014) Stem cells for skeletal muscle regeneration: Therapeutic potential and roadblocks. *Transl Res* 163:409–417.
59. Darabi R, et al. (2012) Human ES- and iPS-derived myogenic progenitors restore DYSTROPHIN and improve contractility upon transplantation in dystrophic mice. *Cell Stem Cell* 10:610–619.
60. Gillies AR, Lieber RL (2011) Structure and function of the skeletal muscle extracellular matrix. *Muscle Nerve* 44:318–331.
61. Webster MT, Manor U, Lippincott-Schwartz J, Fan CM (2016) Intravital imaging reveals ghost fibers as architectural units guiding myogenic progenitors during regeneration. *Cell Stem Cell* 18:243–252.
62. Borschel GH, Dennis RG, Kuzon WM (2004) Contractile skeletal muscle tissue-engineered on an acellular scaffold. *Plast Reconstr Surg* 113:595–602; discussion 603–604.
63. Rossi CA, et al. (2011) In vivo tissue engineering of functional skeletal muscle by freshly isolated satellite cells embedded in a photopolymerizable hydrogel. *FASEB J* 25:2296–2304.
64. Borselli C, Cezar CA, Shvartsman D, Vandenburgh HH, Mooney DJ (2011) The role of multifunctional delivery scaffold in the ability of cultured myoblasts to promote muscle regeneration. *Biomaterials* 32:8905–8914.
65. Levenberg S, et al. (2005) Engineering vascularized skeletal muscle tissue. *Nat Biotechnol* 23:879–884.
66. Boekhoven J, Stupp SI (2014) 25th anniversary article: Supramolecular materials for regenerative medicine. *Adv Mater* 26:1642–1659.
67. Han WM, Jang YC, Garcia AJ (2017) Engineered matrices for skeletal muscle satellite cell engraftment and function. *Matrix Biol* 60–61:96–109.

Downloaded at Palestinian Territory, occupied on December 4, 2021
www.manaraa.com